Dendrochronologia 88 (2024) 126274

Contents lists available at ScienceDirect

Dendrochronologia

journal homepage: www.elsevier.com/locate/dendro

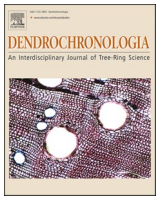

CTRing: An R package to extract wood density profiles from computed tomography images of discs and logs

Dipak Mahatara [a,*], Filipe Campelo [b], Laurent Houle [a], Alain Caron [a], Julie Barrette [c], Pierre Francus [d,e], Robert Schneider [a]

[a] Département de Biologie, Chimie et Géographie, Université du Québec à Rimouski (UQAR), 300 Allée des Ursulines, Rimouski, QC G5L 3A1, Canada
[b] CFE – Centre for Functional Ecology – Science for People & the Planet, Department of Life Sciences, University of Coimbra, Calçada Martim de Freitas, Coimbra 3000-456, Portugal
[c] Direction de la recherche forestière, Ministère des Ressources naturelles et des Forêts, 2700 rue Einstein, Québec G1P 3W8, Canada
[d] INRS – Institut National de la Recherche Scientifique, Centre Eau Terre Environnement, Québec, QC G1K 9A9, Canada
[e] GEOTOP - Research Centre in Earth System Dynamics, Montréal, QC H3C 3P8, Canada

ARTICLE INFO

Keywords:
Automatic detection
Computed tomography
EW–LW transition
Pith
Tree-ring profile

ABSTRACT

Accurately determining the position of pith and accessing tree-ring density profiles, including intra-ring variations, is important for both the forest industry and dendroclimatology. Although several available methods exist for acquiring this information, such as X-ray computed tomography (CT), micro-CT, and X-ray films, the availability of open-source programs for extracting data remains limited. The CTRing package in the R environment integrates a series of functions to detect precisely the pith and tree-ring boundaries and generate tree-ring density profiles using CT images of tree cross sections. Before processing, grey values are transformed into density using a calibration function. Pith position is then detected by combining an adapted Hough Transform method and a one-dimensional edge detector. Tree-ring profiles along the pith-to-bark path of interest are inspected visually, and tree-ring boundaries can be easily added or removed manually via a graphical user interface. After correcting for tree-ring boundaries, the inflection points of a 3rd-degree polynomial obtained from density profiles are used to delimit the earlywood–latewood transition. We tested this package using 60 CT-scanned images of white spruce (*Picea glauca* (Moench) Voss) discs collected at various tree heights (0 %, 25 %, 50 % and 75 % of the total tree height as well as at 1.3 m). The pith detection function had an average mean error of 0.72 mm with 95 % of the automatically detected pith locations that differed by less than 2 mm from their manually located positions. Error decreased toward the apex of the tree. The functions of the CTRing package are flexible and can be easily implemented or adapted. The package could also be used with simple images of discs to obtain ring-width time series; however, this use must be evaluated further. Future work with this package involves assessing the use of low-quality images and ring-porous species.

1. Background

Tree rings are commonly used to understand tree growth dynamics and their response to climate. These growth rings hold information related to the surrounding biotic and abiotic conditions. Cell formation in the rings is first determined by the genetic features of the species and the age of the cambial cells (Harold, 1990; Vaganov et al., 2006; Rathgeber et al., 2016). The number of cells produced in the apical and secondary meristems of a tree is nevertheless regulated by a series of complex interactions between biotic and abiotic factors, including competition, geographic location (e.g., solar radiation, growing season length), wind speed, soil nutrition, soil moisture and climate (Bradley, 1985; Fritts, 2012; Ford et al., 2017; Abedi, 2021; Wu et al., 2022). Temperature and precipitation often limit cell formation and, hence, tree growth (Kozlowski and Pallardy, 1997; Żywiec et al., 2017; Gauli et al., 2022). Thus, tree-ring growth patterns can provide important information about past climatic conditions and indicate whether the trees have experienced favourable or unfavourable conditions over their lifetime (Fritts, 2012; Koprowski, 2013; De Micco et al., 2016; Visser, 2021)

* Corresponding author.
E-mail addresses: dipak.mahatara@uqar.ca (D. Mahatara), fcampelo@ci.uc.pt (F. Campelo), Laurent.Houle@uqar.ca (L. Houle), Alain_Caron@uqar.ca (A. Caron), Julie.Barrette@mffp.gouv.qc.ca (J. Barrette), Pierre.Francus@inrs.ca (P. Francus), Robert_Schneider@uqar.ca (R. Schneider).

https://doi.org/10.1016/j.dendro.2024.126274
Received 20 December 2023; Received in revised form 9 October 2024; Accepted 6 November 2024
Available online 8 November 2024

Over the last few decades, interest has shifted from ring width to ring density profiles for several reasons. Wood density is important for the forest industry and is frequently linked to other wood properties such as the modulus of elasticity and the modulus of rupture (Zobel and Van Buijtenen, 2012; Schneider et al., 2008; Baar et al., 2015; Morel et al., 2018). Wood density, especially when scaled to the entire tree, plays a crucial role in assessing tree and stand biomass and effectively evaluating forest carbon sequestration (Baker et al., 2004; Babst et al., 2014; Pothong et al., 2022). Use of ring density has also increased in dendrochronology primarily because this trait appears more closely correlated with climatic variables than ring width alone. Density-based dendroclimatology relies heavily on the density of latewood (LW), which is formed at the end of the growing season. LW contains a more pronounced climate signal than earlywood (EW, formed at the beginning of the growing season) as it is particularly sensitive to summer climate factors, including temperature and precipitation (Bouriaud et al., 2005; Li et al., 2018; Deng et al., 2022).

Various approaches have been proposed in the literature to measure wood density at both ring and intra-tree ring levels. These methods include the use of beta rays (Phillips, 1960), gamma rays (Woods and Lawhon, 1974), X-rays (Polge, 1966), high-frequency densiometry (Boden et al., 2012), optical method (Dolgova, 2016), and neutron imaging (Mannes et al., 2007). X-ray-based methods stand out as the most widely employed technique for measuring wood density. Often, radiograph films are employed, providing a 2D representation of a 3D object and thereby forfeiting depth information. This approach relies on samples with a defined thickness, and to minimize biases, sample preparation is important. Hounsfield (1973) addressed this issue through tomography: capturing projections from varied angles with a subsequent 3D reconstruction of an object. Since then, X-ray tomography has revolutionized wood imaging, especially for dendrochronological studies or for assessing internal features of tree logs.

The automatic measuring of tree rings is important for obtaining high sample throughputs. The first step is to identify the location of the pith. Although this is the first step in generating radial profiles (Norell, 2009), pith position provides information related to the inner structure of logs, helps detect longitudinal gradients as well as knots and cracks in the wood and allows determining growth-ring eccentricity (Saint-André and Leban, 2001). Numerous techniques have been proposed to facilitate the automated or semi-automated detection of pith position from various image sources, including X-ray tomography, ultrasonic tomography (UT), inexpensive cameras and surface laser scans of tree cross sections. Among these approaches, the Hough Transform (HT) method is commonly applied (Bhandarkar et al., 1999; Andreu and Rinnhofer, 2001; Longuetaud et al., 2004; Norell and Borgefors, 2008; Boukadida et al., 2012). In the HT-based method, growth rings are conceptualized as concentric circles centred around the pith. Some studies have also used the biological or morphological properties of trees to locate the pith (Jaeger et al., 1999; Flood et al., 2003). Wei et al. (2011) and Beaulieu and Dutilleul (2019) provide comprehensive reviews of different pith detection approaches. HT-based methods work very well for small-sized and fast-growing tree species, as they have relatively regular, circular and wide annual rings. However, HT-based methods can produce inaccurate pith locations when the annual rings contain irregularities, defects and decay.

After the pith's location is identified, the following step involves identifying tree-ring edges within the pith-to-bark profile. Most studies have adopted an edge detection approach, in which annual rings are tracked by locating the sharp transition and abrupt changes in the pixel intensity of the image (Cerda et al., 2007; Kalle et al., 2009; Entacher et al., 2007; Sundari and Kumar, 2014). These discontinuities in pixel intensity result from the density change between the dark-coloured LW and the light-coloured EW. Many commercial and freely available tools (e.g., ImageJ, WinDENDRO™, CooRecorder, LignoVision™) can detect and measure tree rings.

Several research groups have developed R packages and algorithms for tree-ring analyses. Hietz (2011) linked the commercial image analysis program SigmaScan with Excel and R code to analyse tree rings. Lara et al. (2015) delineated rings through variations in greyscale values using the measuRing R package through a visual interface. Moreover, Campelo et al. (2019) developed the xRing package, designed specifically for analysing micro-densitometry data, to automatically detect tree-ring boundaries, and this package also provided a graphical user interface (GUI) for manual correction. More recently, Poláček et al. (2023) applied deep learning to detect and measure tree rings automatically, and Martinez-Garcia et al. (2021) developed a new algorithm to visualize the 3D structure of tree rings. To the best of our knowledge, there exists no R package that encompasses functions for automatically identifying pith location, ring segmentation, and computing average ring density for processing the CT-scan data of tree discs and logs. Moreover, these techniques use increment cores or wood samples of fixed thickness to detect and measure tree rings. In contrast, our method can provide a detailed map of tree-ring variations across the entire disc, allowing for the recording of complete growth rings, more accurate estimation of ring areas, and measurement of ring density along several pith-to-bark paths.

In this manuscript, we present CTRing, a new R package that extends the capabilities of the XRing package to X-ray CT images; this novel package includes functions to automatically detect pith, produce a tree-ring density profile, delineate the EW–LW transition and allow for manual corrections. Pith detection is based on the HT method, which uses multiple arc segments; this approach should be robust when encountering defects found within a tree disc. Finally, we present results from samples collected from two plantation-grown white spruce (*Picea glauca* (Moench) Voss) trees.

2. Materials and methods

2.1. Computerized tomography (CT)

CT scans produce a series of X-ray images collected at different angles to enable visualizing an object's internal structures. These images, called projections, are then used to produce a 3D view of the volume using a filtered back projection (Hendee and Ritenour, 2003). The object is described by voxels (e.g., 100 × 100 × 400 μm; in a 3D grid) that contain the attenuation of the X-ray signal. The attenuation is expressed in Hounsfield units (HU) and is calculated as the ratio of X-ray attenuation differences (Kalender, 2011; Vock, 2001)(Eq. 1).

$$HU = 1000\,\frac{\mu_x - \mu_{water}}{\mu_{water} - \mu_{air}} \tag{1}$$

where μ_x, μ_{water} and μ_{air} are the linear attenuation coefficients for the tested specimen (length·unit^{-1}), water (length·unit^{-1}) and air (length·unit^{-1}), respectively. HU is represented by grey levels (recorded at 8, 12 or 16 bits), as shown in Fig. 1, and its values fluctuate with wood density, as the attenuation coefficient is directly related to density (Macedo et al., 2002). To obtain density values, we selected middle slice from all the images in the z-direction, such that the voxels become pixels. Any slice can be used, or the slices can be averaged over the z-direction. The number of pixels per slice is always constant (512 × 512). Thus, the size of the pixel or the image resolution varies with specimen size (between 0.15 and 0.51 mm·pixel^{-1} for our sample discs).

2.2. Method overview

2.2.1. The pith-to-bark profile for a path of interest is obtained by

1. Rescaling the HU values (i.e., grey values between 0 and 255);
2. Applying a calibration curve to obtain density values for each voxel;
3. Identifying the pith of the disc;
4. Selecting the pixels along the pith-to-bark path of interest;

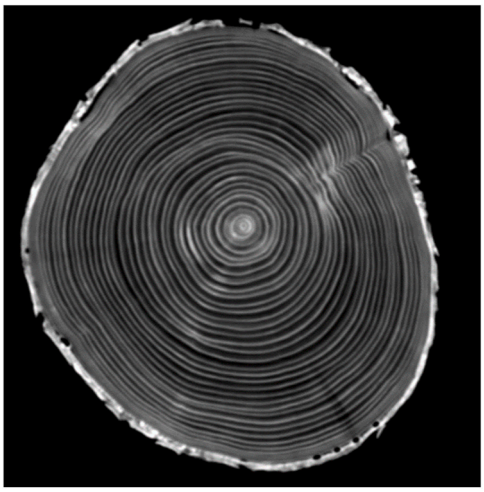

Fig. 1. An X-ray computed tomography image of the cross section of a white spruce log in which the densities at different positions in the object are shown in a greyscale format. The darker zones indicate earlywood, and the lighter ones indicate latewood.

5. Delineating the rings, EW and LW along the path and averaging the density.

All steps were coded in R (R Core Team, 2021) and are presented in the CTRing package. The package is available under the GPL-3 licensing. Each step is detailed in the following subsections.

2.2.2. Rescaling the HU values

CT scanners store HU values as 8-bit (256 levels), 12-bit (4096 levels), or 16-bit (65,536 levels). To ensure portability and homogenize the workflow irrespective of CT scanner capacities, we rescale the grey values (GV_i, where i is the number of bits) between 0 and 255 (GV_8, Eq. 2). The values were not rounded to the integer value (i.e. all the decimals in the converted grayscale representation are kept). The downscaling to the 0–255 range is more convenient than rounding up to 12-bit or 16-bit grey levels, especially for CT scanners that store values in a lower-bit format.

$$GV_8 = GV_i \bullet \frac{2^8}{2^i} \tag{2}$$

2.2.3. Density values

Using the 8-bit grey values of samples of known density (acetal, heatglue, mosa, teflon and ultra-high molecular weight [UHMW] plastic), we developed a linear calibration equation (Fig. 2, intercept = −0.14, slope = 0.018). As X-ray absorption relies on atomic composition, we used calibration materials having composition closely resembling that of wood. All samples were passed through a X-ray CT scanner (Siemens SOMATOM Definition AS+ 128) at INRS-ETE in Quebec City, Quebec. The X-ray tube of the CT scanner was operated at an energy level between 70 and 140 kV and a current of 300–700 mA. The equipment was controlled by a workstation running Syngo CT VA48A software, which was originally designed for medical applications.

2.2.4. Pith identification

2.2.4.1. The location of the pith was found by iterating over several steps.

Step a: From a given point having coordinates *x1*, *y1* (the starting value is the centre of the image and is updated at the end of each iteration), n number of line segments are traced from the centre to the tree-ring limits of the image (Fig. 3a). The length of each line segment is less than half of the smallest dimension of the input image, and two adjacent line segments form an angle of $360/n$ between them.

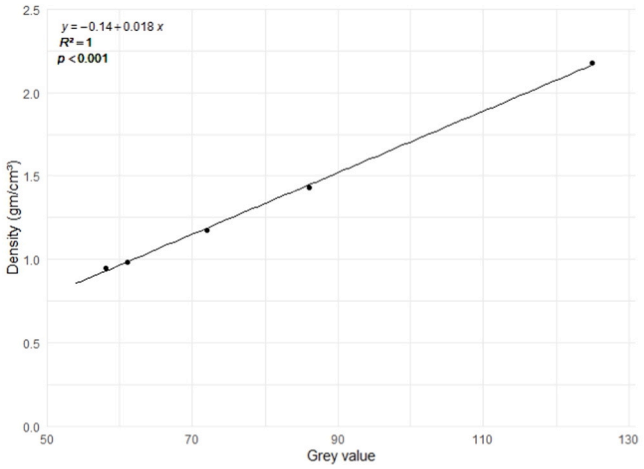

Fig. 2. Calibration curve relating density to 8-bit grey values of known materials.

A density profile for each individual segment is then obtained using a rotated rectangle between two points. The rotated rectangle serves as a moving window, extracting pixel values along the length and width of the rectangle and thus forms a matrix of profiles from the n segments. The length of this rectangle corresponds to the distance between two points.

Step b: The n profiles in the form of a matrix formed in the previous step are used as input for this step. Then, from density profiles, tree-ring edges were detected by adapting the "getBorders()" function from the xRing package (Campelo et al., 2019), which calculates the difference between the local k-point maximum and minimum and compares it to a threshold value, explicitly defined by the user, to identify the tree-ring boundaries (> threshold). The function simulates the kernel of the edge detectors, albeit in a horizontal 1D form. The argument k provides the length of the moving window used to calculate the local extreme values.

Step c: A new estimate of pith location is then obtained by using tree-ring edges. Our proposed technique is a modification of the original HT method. In the HT approach, the algorithm considers tree rings as a set of concentric circles, whereas our technique focuses on identifying the closest pairs of points from two adjacent segments (Fig. 3b). We hypothesized that the closest points between two adjacent segments likely belong to the same tree-ring border. Thus, these pairs of points generate numerous arcs that should have the same centre, i.e., the tree pith. Geometrically, the perpendicular line that bisects the line segment connecting two endpoints of an arc passes from the center of the circle, of which that arc is a segment (Fig. 3c). Thus, the pith is then estimated as the intersection of all the lines obtained by the bisections of arcs (Fig. 3d). The pith is assumed to be at the centroid of the intersections of all possible pairs of bisectors after outliers have been discarded by removing intersecting points outside the main cloud of points (Fig. 3e).

Steps a to c are repeated (using the new estimate of pith location) until the previous coordinates are found or the maximum number of iterations (30) is reached.

2.2.5. Selecting the pixels along the pith-to-bark path of interest

The path corresponding to n-pixels wide is defined by the coordinates of the pith and an endpoint selected by the user (Fig. 4a). The width of the line is set, and an average density perpendicular to the path is calculated to obtain the pith-to-bark density profile (Fig. 4b).

2.2.6. Delineating the rings, earlywood and latewood along the path and averaging the density

Segmenting the profile path to rings relies on using a modified version of the "getBorders()" function from the xRing package, as

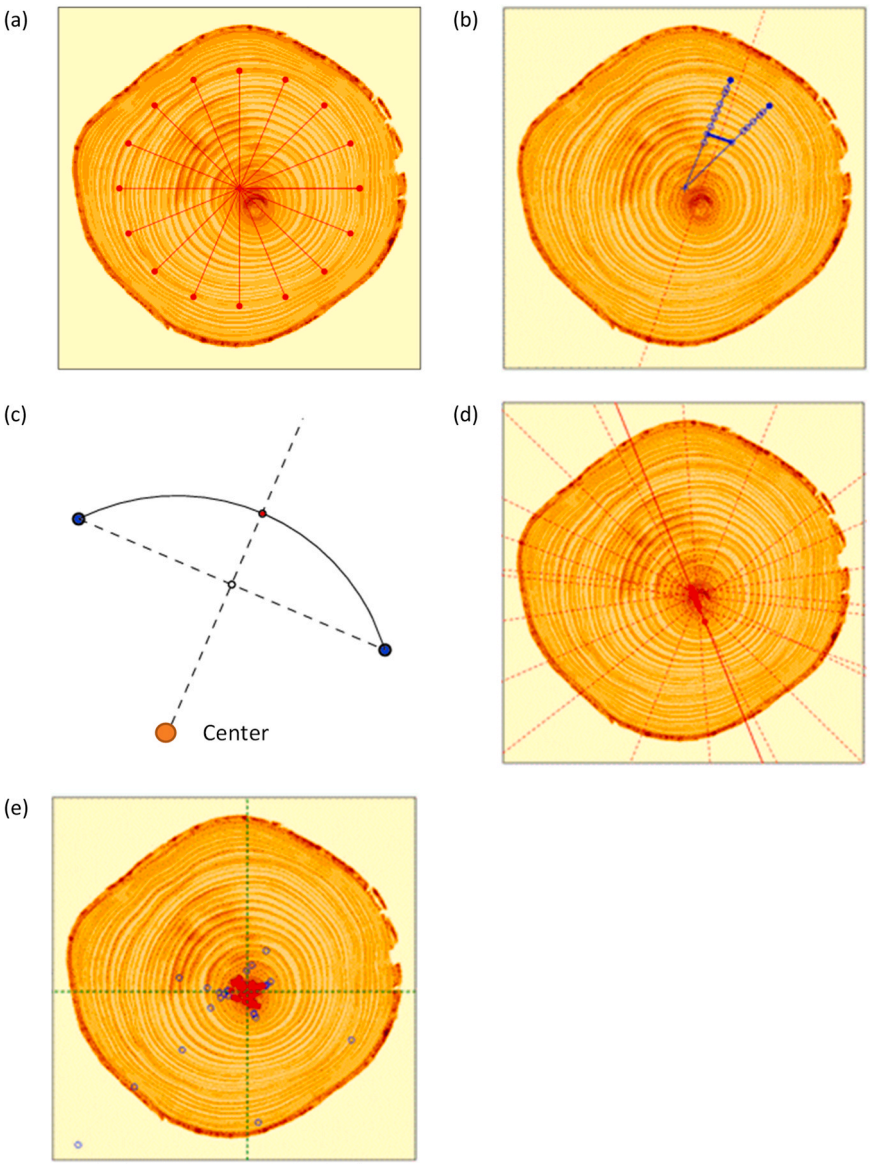

Fig. 3. (a) Initial estimate of the pith location and segmentation of the image from pith location; (b) the location of two ring-edge points from adjacent segments; (c) estimation of the new pith based on the principle that the perpendicular bisector of any arc of a circle passes through the centre of the circle; (d) number of bisectors along which the pith should be located; and (e) positions for the pith estimated as the intersection of two bisectors (in figure e, blue points are considered outliers and red points are used to estimate the pith location; the intersection of the green dotted lines indicates the estimated pith location).

discussed above. After the profile is segmented, the delineation of rings is confirmed visually. The ring count calculated using the "getBorders()" function is subsequently compared with the manually counted rings on the disc or DICOM image. Rings are then added or removed accordingly using a graphical user interface (GUI).

The EW–LW transition is obtained using a 3rd-degree polynomial that is fitted to the density profile of each ring (Eq. 3).

$$density = a + b \bullet dist + c \bullet dist^2 + d \bullet dist^3 + \varepsilon \quad (3)$$

where a, b, c and d are the parameters estimated by the regression, $dist$ represents the distance from the pith (in mm) and ε is the residual error.

The inflection point (e.g., $-2c/6d$) of the polynomial is assumed to correspond to the transition point between the EW and LW in the case that the polynomial is of the convex–concave form (Fig. 5a). If the polynomial method fails, for instance, in cases with a low number of points within the ring, or when the minimum and maximum values fall outside the expected range, or when the inflection point is close to the minimum or maximum density of the ring, we use the mid-point method. In mid-point method, the EW-LW transition is established as the distance to the midway point between the minimum and maximum density of the ring (Fig. 5b). Similarly, for the concave-convex polynomial form, the transition is determined as the distance to the midpoint between the minimum and maximum density of the ring (Fig. 5c). Table 1 provides the approximate rates at which each transition type is encountered.

Furthermore, the pixel size enables the determination of ring width. Thus, the final data frame for the selected path contains information about the age of the rings, average ring density, ring width, and the densities and widths for both EW and LW.

2.3. CT scan data

We destructively sampled 140 white spruce trees from two plantations established in the year 1990. Within each tree, five 2 cm thick discs were extracted at 0 %, 25 %, 50 % and 75 % of the total height, as well as at a fixed height of 1.3 m. These discs were preserved in a freezer until

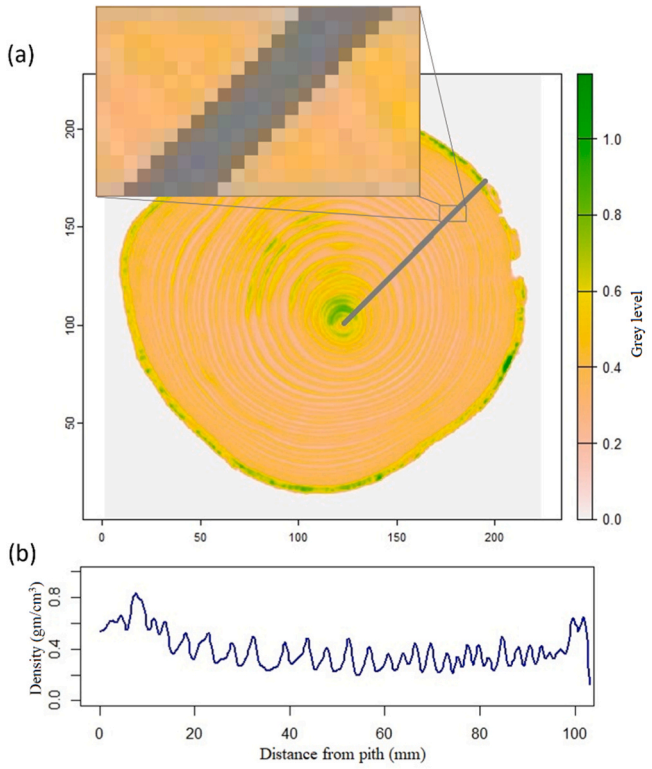

Fig. 4. Profile path on the raster image, highlighting (a) the pixels through which the profile passes and (b) the plot of the profile from pith to the bark of the selected path.

processing. Before undergoing scanning, the discs were placed in a conditioning room at a temperature of 20–22 °C and 65 % relative humidity until constant weight was reached, implying a 12 % moisture content (ISO 554, 2002). The samples were scanned in the same CT scanner using the same settings as those used for obtaining the calibration curve data set.

2.3.1. *Validation of pith location*

To assess the pith location functions, we randomly selected 60 sample discs representing all heights (0 %, 25 %, 50 %, and 75 % of the total height, as well as at 1.3 m) and social classes. The sample trees had an average diameter, height and age of 18.37 cm, 13.35 m and 31 years, respectively. The automatically identified pith (x_1, y_1) was compared against the actual pith position (x_0, y_0), the latter obtained by manual inspection of the CT images. We then calculated discrepancies (i.e., errors or distance from the actual pith (0, 0) in arbitrary *x*- and *y*-axes) and the Euclidean distance between the actual pith and automatically

Table 1
Earlywood-latewood Transition types of the annual rings in percentage for the 60-disc samples representing different heights.

Disc height	Transition type (in percentage)				
	1	2	3	4	5
0 %	14.8	47.9	5.9	29.0	2.4
1.3 m	4.1	78.2	4.8	12.9	0
25 %	1.7	77.4	7.8	13.1	0
50 %	1.1	86.0	4.3	8.6	0
75 %	4.6	92.3	1.5	1.6	0

Transition types: 1 denotes a low number of points in the ring; 2 denotes the inflection point estimated by polynomial; 3 denotes minimum or maximum out of range; 4 denotes inflection point close to minimum or maximum; 5 denotes convex to concave. The disc samples used here are the same ones used to validate the pith location.

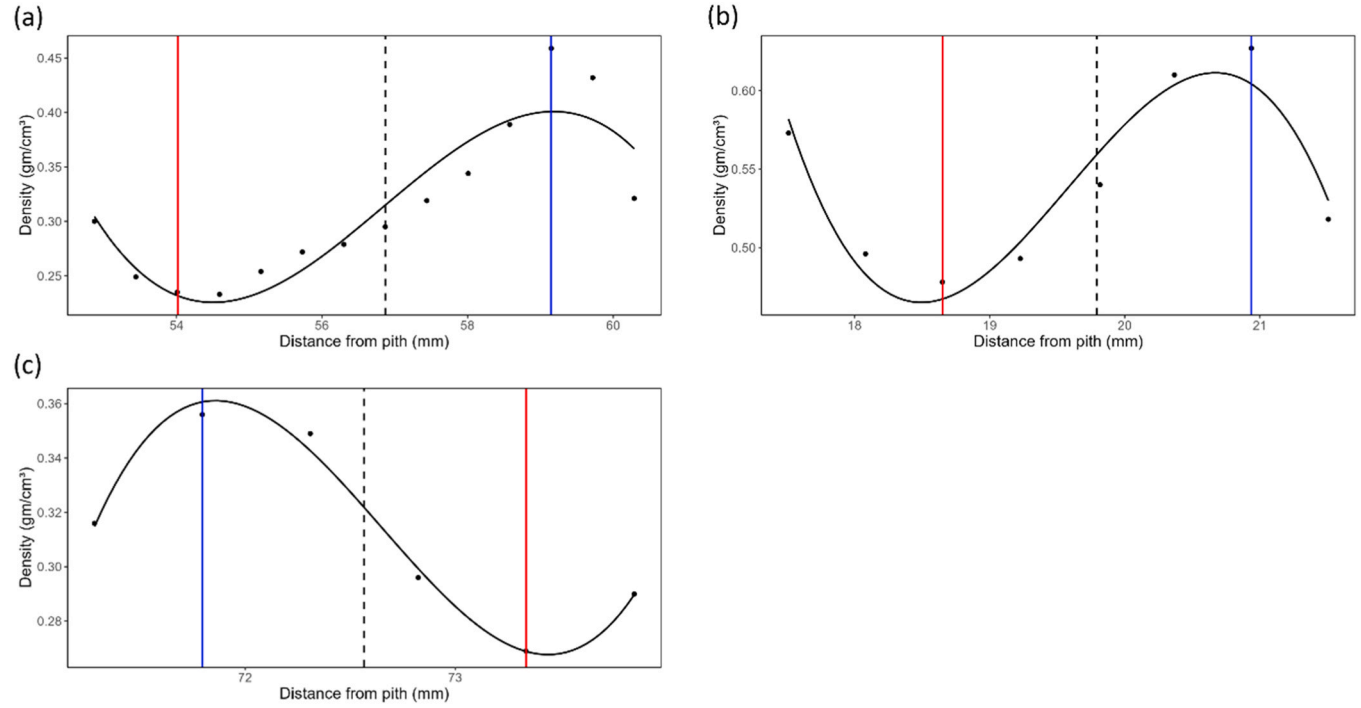

Fig. 5. Earlywood-latewood transition (a) established by polynomial method, (b) established by mid-point method when there are a low number of points within the ring, or when the minimum and maximum values fall outside the expected range, or when the inflection point is close to the minimum or maximum density of the ring and (c) established by mid-point method when the polynomial is concave-convex form. The black line is the fitted 3rd degree polynomial function; the red and blue solid lines indicate the minimum and the maximum density points, respectively and the black dashed line indicates the transition point between earlywood-latewood.

located pith (ED, Eq. 4):

$$ED = \sqrt{(x_1 - x_0)^2 + (y_1 - y_0)^2} \quad (4)$$

3. Results

The largest errors were observed for samples collected at the tree base—0 % height—1.4 mm and 3.5 mm in the x- and y-directions, respectively (Fig. 6a). Fig. 6b shows that more than two-thirds of the automatically detected pith was less than 1 mm from their manually located position and that the ED of 95 % of the discs was less than 2 mm. Notably, the three sample discs featuring an ED above the 2 mm threshold exhibited more pronounced irregularities within the ring structures. In regard to ED variation with height within the tree (Fig. 6c), pith detection accuracy increased from the stump to the apex of the tree. The average ED of the discs at 75 % was 0.42 mm, compared with 1.26 mm at 0 %.

4. Discussion

The CTRing package integrates three main steps to extract the tree-ring information from the CT-scan images: automatic detection of the pith, automatic delineation of tree rings and a graphical user interface (GUI) to correct the pith location and tree-ring edges. The good predictive performance, user-friendly interface and relatively fast processing times make CTRing package a reliable alternative for CT-image analysis in dendrochronology and forest ecology.

We demonstrated that the developed algorithm located efficaciously the pith of various tree sizes and at different heights within the tree. Detection accuracy was lowest for discs collected closest to the stem base, as these samples exhibited more irregularities and "defects" in the tree-ring edges. Moreover, the number of pixels of an image is constant; thus, the pixels cover larger areas for the larger discs. Furthermore, in the upper stem of the tree, the annual rings become wider and more regular, and it is easier to obtain defect-free discs in the upper stem. Boukadida et al. (2012) reported errors in pith detection for hardwood species related to secondary pith produced by forking at the top of the tree. This scenario may not be true for most softwood species, as they tend to have a single, dominant straight trunk with small side branches.

Overall, our mean discrepancy was 0.72 mm compared to 4.19 mm in Andreu and Rinnhofer (2001), 0.75 mm in Longuetaud et al. (2004), 1.69 mm in Boukadida et al. (2012) and 4.18 mm in Gazo et al. (2020), all using the HT method run on CT-scan data. Furthermore, in a related study, Habite et al. (2020) reported a mean error of 2.6 mm along the x-axis and 3.2 mm along the y-axis whereas, Perlin et al. (2018) observed an overall error of 5 mm when using images acquired through optical surface scanning and ultrasonic measurements, respectively. By using arcs rather than the complete ring, our method reduces the effect of possible abnormalities on estimates of pith location, thereby increasing the accuracy for the images with defects, broken rings or where the ring direction changes rapidly and/or frequently. The accuracy of our method could be further improved by changing the settings or discarding those discs with obvious defects.

We applied a third-degree polynomial to delimit the EW–LW transition. The most widely used methods for identifying this zone are threshold densities, Mork's Index (MI) and the inflection-point method.

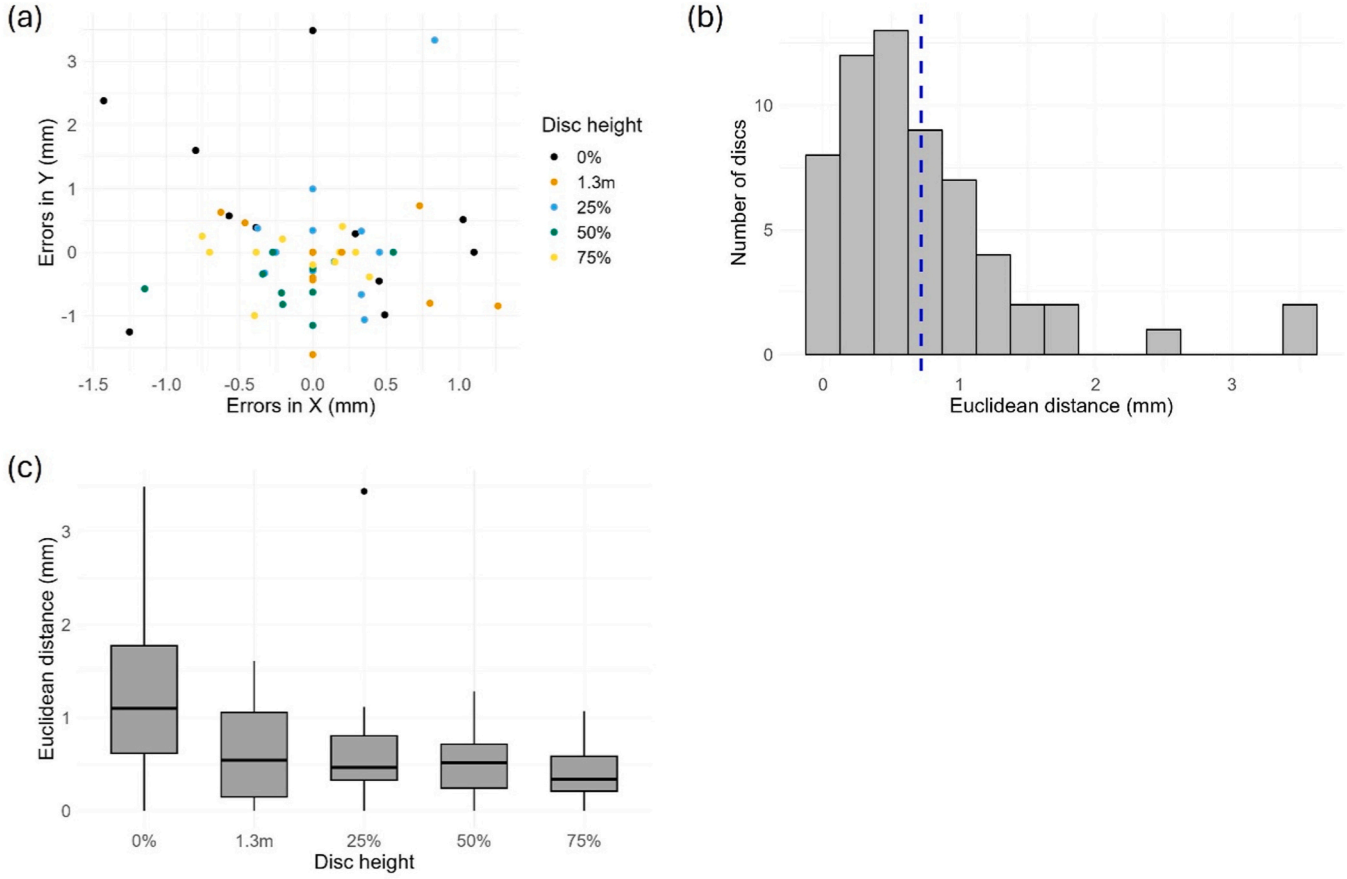

Fig. 6. (a) Distances between the automatically and manually detected locations of pith in the x- and y-direction in terms of error (we considered all manually detected pith locations as 0, 0); (b) histograms showing the Euclidean distance between manually and automatically determined pith locations. The blue dashed line denotes the mean value (0.72 mm). (c) Boxplots presenting the Euclidean distances between manually and automatically determined pith locations for different disc heights.

Threshold density relies on an arbitrary threshold value of wood density used to delimit EW and LW (Kumar, 2002). For example, Cown and Ball (2001) applied a threshold density of 400 $kg \cdot m^{-3}$ to define the EW–LW transition in Monterey (radiata) pine (*Pinus radiata* D. Don). Other studies have defined the EW–LW transition as the point where the density surpasses the halfway point between the minimum and maximum density values of a ring (Polge, 1978; Campelo et al., 2019). The first method is a more static approach, as it is based on a single predefined value for all rings, whereas the second method uses two density values (minimum and maximum) that vary from ring to ring and can lead to an EL–LW transition at quite different density values. On the other hand, MI is an anatomically based approach (Mork, 1928), which considers the wall thickness of the tracheid to define both types of wood. MI involves identifying the features (cell lumen diameter and cell wall thickness) of individual tracheids within a tree ring, thereby producing comprehensive anatomical data sets (Samusevich et al., 2020). When within-ring density varies substantially, both the threshold and MI approaches often misidentify the transition point (Björklund et al., 2017). Also, it was found that both methods tended to overestimate the proportion of EW, particularly for rings near the pith (Koubaa et al., 2002; Antony et al., 2012). All methods can erroneously identify the EW–LW transition when intra-annual density fluctuations (IADFs) are present.

Inflection-point methods, also known as derivative methods, rely on identifying points where the density vs. distance from the pith exhibits a change in slope for each individual ring. The inflection point is defined as the maximum of the derivative function that describes the variability of intra-ring density (Koubaa et al., 2002). This point can be established by a polynomial or smooth function (Barbour et al., 1997; Koubaa et al., 2002) or through segmented regression (Nocetti et al., 2011; Franceschini et al., 2013). In our study, we opted for a third-degree polynomial rather than segmented regression because of the substantially lower number of measurements per ring compared with those obtained through micro-densitometry.

The profile is segmented into rings by comparing a threshold value with the minimum and maximum local *k*-points. The sensitivity can thus be adjusted but rarely permits identifying all the rings, by either over- or underdetecting ring transitions. Narrow rings or wide rings having minimal LW (as in juvenile wood) are harder to segment because of the low contrast between the LW and EW of adjacent rings. IADFs or false rings—where short-term climate events cause tracheids having larger cell walls to be produced during EW forming (Palakit et al., 2012)—or cracks produced because of conditioning constraints can be inadequately detected. Therefore, correcting these possible errors in tree-ring edges and EW–LW transitions requires visually verifying these areas and then correcting manually; our package can perform these adjustments.

Further work should include improving the tree-ring detection accuracy of the CTRing package by controlling for multiple sources of noise. Moreover, noise that may arise from complex anatomical features could be reduced through image filtering, and thresholding could be applied to segment those images having a poor resolution (Sauvola and Pietikäinen, 2000). Threshold-based segmentation acts as a selective filter by isolating tree-ring features from the background, thus allowing for precise analysis even when using distorted images with noise.

CTRing works well for white spruce, with the estimated pith location differing minimally from the observed position. It would be interesting to validate the package on species that lack distinct ring transitions, i.e., diffuse-porous species such as sugar maple (*Acer saccharum*) and trembling aspen (*Populus tremuloides*), or for species having less stable edges, such as European ash (*Fraxinus excelsior*) (Fabijańska et al., 2017).

Author contributions

Dipak Mahatara, Robert Schneider, and Filipe Campelo conceived the ideas and led the package development; Dipak Mahatara led the writing of the manuscript and Robert Schneider supervised the work; All authors worked on the advancement of the package, contributed critically to the draft, and gave final approval for the submission. The authors declare no conflict of interest.

Declaration of Competing Interest

The authors declare that they have no known competing financial interests or personal relationships that could have appeared to influence the work reported in this paper.

Acknowledgments

Funding was provided by Forest research service contract number 3329–2019–142332176-B obtained by Robert Schneider from the Ministère des Ressources naturelles et des Forêts (Quebec, Canada), and the Natural Sciences and Engineering Research Council of Canada. The authors would like to acknowledge Laval University and Institut National de la Recherche Scientifique, Québec for their support during sample storage and processing. We thank our reviewers for their comprehensive and insightful feedback, which greatly enhanced both the quality of this paper and the package.

Data Availability

The source code is available at https://gitlab.uqar.ca/schnro01/ctring and the CTRing package can be downloaded from the Comprehensive R Archive Network website (CRAN: https://cran.r-project.org/web/packages/CTRing).

References

Abedi, T. (2021). Effects of Some Important Genes, Phytohormones, and Abiotic Factors on Wood Formation in Trees, An Overview.

Andreu, J.P., Rinnhofer, A., 2001. Automatic Detection of Pith and Annual Rings on Industrial Computed Tomography Log Images Scantech, Seattle, Wash., USA3747.

Antony, F., Schimleck, L.R., Daniels, R.F., 2012. A comparison of earlywood–latewood demarcation methods–a case study in loblolly pine. IAWA J. 33 (2), 187–195.

Baar, J., Tippner, J., Rademacher, P., 2015. Prediction of mechanical properties-modulus of rupture and modulus of elasticity-of five tropical species by nondestructive methods. Maderas Cienc. Y. Tecnol. ía 17 (2), 239–252.

Babst, F., Bouriaud, O., Papale, D., Gielen, B., Janssens, I.A., Nikinmaa, E., Ibrom, A., Wu, J., Bernhofer, C., Köstner, B., 2014. Above-ground woody carbon sequestration measured from tree rings is coherent with net ecosystem productivity at five eddy-covariance sites. N. Phytol. 201 (4), 1289–1303.

Baker, T.R., Phillips, O.L., Malhi, Y., Almeida, S., Arroyo, L., Di Fiore, A., Erwin, T., Killeen, T.J., Laurance, S.G., Laurance, W.F., 2004. Variation in wood density determines spatial patterns in Amazonian forest biomass. Glob. Change Biol. 10 (5), 545–562.

Beaulieu, J., Dutilleul, P., 2019. Applications of computed tomography (CT) scanning technology in forest research: a timely update and review. Can. J. For. Res. 49 (10), 1173–1188.

Bhandarkar, S.M., Faust, T.D., Tang, M., 1999. CATALOG: a system for detection and rendering of internal log defects using computer tomography. Mach. Vis. Appl. 11 (4), 171–190.

Björklund, J., Seftigen, K., Schweingruber, F., Fonti, P., von Arx, G., Bryukhanova, M.V., Cuny, H.E., Carrer, M., Castagneri, D., Frank, D.C., 2017. Cell size and wall dimensions drive distinct variability of earlywood and latewood density in Northern Hemisphere conifers. N. Phytol. 216 (3), 728–740.

Boden, S., Schinker, M.G., Duncker, P., Spiecker, H., 2012. Resolution abilities and measuring depth of high-frequency densitometry on wood samples. Measurement 45 (7), 1913–1921.

Boukadida, H., Longuetaud, F., Colin, F., Freyburger, C., Constant, T., Leban, J.M., Mothe, F., 2012. PithExtract: a robust algorithm for pith detection in computer tomography images of wood–Application to 125 logs from 17 tree species. Comput. Electron. Agric. 85, 90–98.

Bouriaud, O., Leban, J.-M., Bert, D., Deleuze, C., 2005. Intra-annual variations in climate influence growth and wood density of Norway spruce. Tree Physiol. 25 (6), 651–660.

Bradley, R.S. (1985). Quaternary Paleoclimatology; Methods of Paleoclimatic Reconstruction. Quaternary Paleoclimatology; Methods of Paleoclimatic Reconstruction. https://doi.org/10.2307/632972.

Campelo, F., Mayer, K., Grabner, M., 2019. xRing—An R package to identify and measure tree-ring features using X-ray microdensity profiles. Dendrochronologia 53, 17–21.

Cerda, M., Hitschfeld-Kahler, N., Mery, D., 2007. Robust tree-ring detection. Pac. Rim Symp. Image Video Technol. 575–585.

Cown, D.J., Ball, R.D., 2001. Wood densitometry of 10 Pinus radiata families at seven contrasting sites: influence of tree age, site, and genotype. N. Z. J. For. Sci. 31 (1), 88–100.

De Micco, V., Campelo, F., De Luis, M., Bräuning, A., Grabner, M., Battipaglia, G., Cherubini, P., 2016. Intra-annual density fluctuations in tree rings: how, when, where, and why? IAWA J. 37 (2), 232–259.
Deng, G., Li, M., Hao, Z., Shao, X., 2022. Responses to climate change of maximum latewood density from Larix speciosa Cheng et Law and Abies delavayi Franch. in the Northwest of Yunnan Province. China For. 13 (5), 720.
Dolgova, E., 2016. June–September temperature reconstruction in the Northern Caucasus based on blue intensity data. Dendrochronologia 39, 17–23.
Entacher, K., Planitzer, D., Uhl, A., 2007. Towards an automated generation of tree ring profiles from CT-images. 2007 5th Int. Symp. Image Signal Process. Anal. 174–179.
Fabijańska, A., Danek, M., Barniak, J., Piórkowski, A., 2017. Towards automatic tree rings detection in images of scanned wood samples. Comput. Electron. Agric. 140, 279–289.
Flood, K., Danielsson, P.E., Seger, M.M., 2003. On 3D Segmentation of Knots in 3D-Volume Data Acquired From X-ray Linear Cone-beam Scanning, Fifth Int. Conf. Image Process. Scanning Wood 2326.
Ford, K.R., Breckheimer, I.K., Franklin, J.F., Freund, J.A., Kroiss, S.J., Larson, A.J., Theobald, E.J., HilleRisLambers, J., 2017. Competition alters tree growth responses to climate at individual and stand scales. Can. J. For. Res. 47 (1), 53–62.
Franceschini, T., Longuetaud, F., Bontemps, J.-D., Bouriaud, O., Caritey, B.-D., Leban, J.-M., 2013. Effect of ring width, cambial age, and climatic variables on the within-ring wood density profile of Norway spruce Picea abies (L.) Karst. Trees 27, 913–925.
Fritts, H. (2012). Tree Rings and Climate. Elsevier.
Gauli, A., Neupane, P.R., Mundhenk, P., Köhl, M., 2022. Effect of climate change on the growth of tree species: dendroclimatological analysis. Forests 13 (4), 496.
Gazo, R., Vanek, J., Abdul_Massih, M., Benes, B., 2020. A fast pith detection for computed tomography scanned hardwood logs. Comput. Electron. Agric. 170, 105107.
Habite, T., Olsson, A., Oscarsson, J., 2020. Automatic detection of pith location along norway spruce timber boards on the basis of optical scanning. Eur. J. Wood Wood Prod. 78 (6), 1061–1074.
Harold, F.M., 1990. To shape a cell: an inquiry into the causes of morphogenesis of microorganisms. Microbiol. Rev. 54 (4), 381–431.
Hendee, W.R., & Ritenour, E.R. (2003). Medical Imaging Physics. John Wiley & Sons.
Hietz, P., 2011. A simple program to measure and analyse tree rings using Excel, R and SigmaScan. Dendrochronologia 29 (4), 245–250.
Hounsfield, G.N., 1973. Computerized transverse axial scanning (tomography): Part 1. Description of system. Br. J. Radiol. 46 (552), 1016–1022.
ISO 554. (2002). Standard Atmospheres for Conditioning And/or Testing – Specifications.
Jaeger, M., Leban, J.-M., Borianne, P., Chemouny, S., & Saint André, L. (1999). 3D Stem Reconstruction from CT Scan Exams. From Log External Shape to Internal Structures.
Kalender, W.A. (2011). Computed Tomography: Fundamentals, System Technology, Image Quality, Applications. John Wiley & Sons.
Kalle, M., Petteri, O., & Martti, M. (2009). Spectral Reflectances of Log Ends for Camera Based Annual Ring Width Measurments.
Koprowski, M., 2013. Spatial distribution of introduced Norway spruce growth in lowland Poland: the influence of changing climate and extreme weather events. Quat. Int. 283, 139–146.
Koubaa, A., Zhang, S.Y.T., Makni, S., 2002. Defining the transition from earlywood to latewood in black spruce based on intra-ring wood density profiles from X-ray densitometry. Ann. For. Sci. 59 (5–6), 511–518.
Kozlowski, T.T., & Pallardy, S.G. (1997). Growth Control in Woody Plants. Elsevier.
Kumar, S., 2002. Earlywood-Latewood demarcation criteria and their effect on genetic parameters of growth ring density components and efficiency of selection for end-of-rotation density of Radia Pine. Silvae Genet. 51 (5–6), 241–245.
Lara, W., Bravo, F., Sierra, C.A., 2015. measuRing: an R package to measure tree-ring widths from scanned images. Dendrochronologia 34, 43–50.
Li, M., Duan, J., Wang, L., Zhu, H., 2018. Late summer temperature reconstruction based on tree-ring density for Sygera Mountain, southeastern Tibetan Plateau. Glob. Planet. Change 163, 10–17.
Longuetaud, F., Leban, J.-M., Mothe, F., Kerrien, E., Berger, M.-O., 2004. Automatic detection of pith on CT images of spruce logs. Comput. Electron. Agric. 44 (2), 107–119.
Macedo, A., Vaz, C.M.P., Pereira, J.C.D., Naime, J.M., Cruvinel, P.E., & Crestana, S. (2002). Wood Density Determination by X-and Gamma-ray tomography.
Mannes, D., Lehmann, E., Cherubini, P., Niemz, P., 2007. Neutron imaging versus standard X-ray densitometry as method to measure tree-ring wood density. Trees 21, 605–612.
Martinez-Garcia, J., Stelzner, I., Stelzner, J., Gwerder, D., Schuetz, P., 2021. Automated 3D tree-ring detection and measurement from X-ray computed tomography. Dendrochronologia 69, 125877.
Morel, H., Lehnebach, R., Cigna, J., Ruelle, J., Nicolini, E.A., Beauchêne, J., 2018. Basic wood density variations of Parkia velutina Benoist, a long-lived heliophilic Neotropical rainforest tree. Bois Et. êts Des. Trop. 335 (1), 59–69.
Mork, E., 1928. Die qualitaat des fichtenholzes unter besonderer rucsichtnahme auf schleif-und papierholz. Pap. Fabr. 26, 741–747.
Nocetti, M., Rozenberg, P., Chaix, G., Macchioni, N., 2011. Provenance effect on the ring structure of teak (Tectona grandis Lf) wood by X-ray microdensitometry. Ann. For. Sci. 68, 1375–1383.
Norell, K., 2009. An automatic method for counting annual rings in noisy sawmill images. Int. Conf. Image Anal. Process. 307–316.
Norell, K., Borgefors, G., 2008. Estimation of pith position in untreated log ends in sawmill environments. Comput. Electron. Agric. 63 (2), 155–167.
Palakit, K., Siripattanadilok, S., Duangsathaporn, K., 2012. False ring occurrences and their identification in teak (Tectona grandis) in north-eastern Thailand. J. Trop. For. Sci. 387–398.
Perlin, L.P., do Valle, Â., de Andrade Pinto, R.C., 2018. New method to locate the pith position in a wood cross-section based on ultrasonic measurements. Constr. Build. Mater. 169, 733–739.
Phillips, E.W.J., 1960. The beta ray method of determining the density of wood and the proportion of summer wood. J. Inst. Wood Sci. 5, 16–28.
Poláček, M., Arizpe, A., Hüther, P., Weidlich, L., Steindl, S., Swarts, K., 2023. Automation of tree-ring detection and measurements using deep learning. Methods Ecol. Evol. 14 (9), 2233–2242.
Polge, Hubert, 1966. Établissement des courbes de variation de la densité du bois par exploration densitométrique de radiographies d'échantillons prélevés à la tarière sur des arbres vivants: applications dans les domaines Technologique et Physiologique. Ann. Des. Sci. For. èRes 23 (1). I–206.
Polge, H., 1978. Fifteen years of wood radiation densitometry. Wood Sci. Technol. 12 (3), 187–196.
Pothong, T., Elliott, S., Chairuangsri, S., Chanthorn, W., Shannon, D.P., Wangpakapattanawong, P., 2022. New allometric equations for quantifying tree biomass and carbon sequestration in seasonally dry secondary forest in northern Thailand. N. For. 53, 17–36.
R Core Team, 2021. A Language and Environment for Statistical Computing. R Foundation for Statistical Computing, Vienna, Austria. Http://Www.R-Project.Org/.
Rathgeber, C.B.K., Cuny, H.E., Fonti, P., 2016. Biological basis of tree-ring formation: a crash course. Front. Plant Sci. 7, 734.
Saint-André, L., Leban, J.-M., 2001. A model for the position and ring eccentricity in transverse sections of Norway spruce logs. Eur. J. Wood Wood Prod. 59 (1–2), 137–144.
Samusevich, A., Lexa, M., Vejpustková, M., Altman, J., Zeidler, A., 2020. Comparison of methods for the demarcation between earlywood and latewood in tree rings of Norway spruce. Dendrochronologia 60, 125686.
Sauvola, J., Pietikäinen, M., 2000. Adaptive document image binarization. Pattern Recognit. 33 (2), 225–236.
Schneider, R., Zhang, S.Y., Swift, D.E., Begin, J., Lussier, J.-M., 2008. Predicting selected wood properties of jack pine following commercial thinning. Can. J. For. Res. 38 (7), 2030–2043.
Sundari, P.M., Kumar, S.B.R., 2014. An approach for dendroclimatology using image processing techniques. 2014 World Congr. Comput. Commun. Technol. 234–236.
Vaganov, E.A., Hughes, M.K., Shashkin, A.V., 2006. Introduction and factors influencing the seasonal growth of trees. Growth Dyn. Conifer. Tree Rings: Images Future Environ. 1–20.
Visser, R.M., 2021. Dendrochronological provenance patterns. network analysis of tree-ring material reveals spatial and economic relations of Roman timber in the continental North-Western provinces. J. Comput. Appl. Archaeol. 4 (1).
Vock, P., 2001. WA Kalender: Computed tomography: fundamentals, system technology, image quality, applications (with CD-ROM). Eur. Radiol. 11 (9), 1855.
Wei, Q., Leblon, B., La Rocque, A., 2011. On the use of X-ray computed tomography for determining wood properties: a review. Can. J. For. Res. 41 (11), 2120–2140.
Woods, F.W., Lawhon, W.T., 1974. Gamma densitometry of increment cores. For. Sci. 20 (3), 269–271.
Wu, Z., Fan, C., Zhang, C., Zhao, X., von Gadow, K., 2022. Effects of biotic and abiotic drivers on the growth rates of individual trees in temperate natural forests. For. Ecol. Manag. 503, 119769.
Zobel, B.J., & Van Buijtenen, J.P. (2012). Wood variation: its causes and control. Springer Science & Business Media.
Żywiec, M., Muter, E., Zielonka, T., Delibes, M., Calvo, G., Fedriani, J.M., 2017. Long-term effect of temperature and precipitation on radial growth in a threatened thermo-Mediterranean tree population. Trees 31, 491–501.